Available online at www.sciencedirect.com
ScienceDirect
Trans. Nonferrous Met. Soc. China 35(2025) 684−700
Transactions of Nonferrous Metals Society of China
www.tnmsc.cn

Evolution of precipitates and mechanical properties of T6-treated and thermally exposed WAAM-ZL205A alloy

Hai-jiang LIU[1], Yan FENG[1,2], Chao-qun PENG[1,2], Zhi-yong CAI[1,2], Meng WANG[1], Zi-ming LI[1], Zhi-jie KANG[1], Xiao-di ZHANG[1]

1. School of Materials Science and Engineering, Central South University, Changsha 410083, China;
2. National Key Laboratory of Science and Technology on High-strength Structural Materials, Central South University, Changsha 410083, China

Received 15 August 2023; accepted 25 April 2024

Abstract: The microstructure and mechanical properties of the WAAM-ZL205A alloy were investigated at various thermal exposure temperatures and compared with those of the deposited and T6-treated alloys. Due to the precipitation strengthening of fine and scattered θ'' and θ' phases, the yield strength (YS) of the T6-treated ((535 °C, 10 h) + (175 °C, 10 h)) alloy increases to 366.9 MPa compared with that of the deposited alloy. However, the elongation (El) is reduced to 12.9%. When the thermal exposure temperature increases from 200 to 300 °C, there is a notable decrease in YS and the time required to stabilize is shortened. After thermal exposure at 300 °C for 24 h, part of the θ' precipitate located at the grain boundary transforms into the θ phase, while the θ' precipitate within the grains experiences coarsening, resulting in a decrease in YS to 188.9 MPa. Upon surpassing an exposure duration of 120 h, the mechanical characteristics exhibit stability.

Key words: ZL205A Al alloy; precipitate; mechanical properties; additive manufacturing; heat treatment; thermal exposure; stability

1 Introduction

Additive manufacturing (AM), commonly referred to as 3D printing or rapid forming, offers benefits such as material conservation, substantial reduction in lead time, and enhanced feasibility in the production of complex components [1]. In recent years, metal AM has garnered significant interest in the field of advanced manufacturing [2−4]. To lower manufacturing expenses and fabricate intricate components, scholars have utilized AM technology to develop high-performance aluminum alloys that meet with commercial demands [5,6]. Wire arc additive manufacturing (WAAM) is a vital metal AM technology that addresses challenges associated with expensive equipment, limited product dimensions, and slow deposition rates [7]. The WAAM utilizes metal wire as the raw materials and arc as the heat source to deposit metal components layer by layer [8,9]. LI et al [10] developed the cold metal transfer (CMT) technology by adapting the gas metal arc welding (GMAW) process. CMT has the advantages of low heat input and spatter-free and is considered a crucial technique for fabricating aluminum alloy components.

Al−Cu alloys are widely utilized in the aerospace and automobile industries for their light-weight, high specific strength, favorable ductility, and exceptional corrosion resistance [11−14]. The optimization of microstructure and enhancement of

Corresponding author: Meng WANG, Tel: +86-18711150315, E-mail: meng.wang@csu.edu.cn
DOI: https://doi.org/10.1016/S1003-6326(24)66708-7

mechanical properties of Al−Cu alloys can be achieved through heat treatment methods. Among these, quenching and aging processes are popularly employed for precipitation strengthening in Al−Cu alloys, with a precipitation sequence involving GP zone → θ'' → θ' → θ (Al_2Cu) [15]. The shape and volume fraction of θ'' and θ' precipitates play a crucial role in determining the mechanical properties. Studies have been conducted to calculate the strength contribution of θ'' precipitates in WAAM 2219 Al alloy at varies solid solution temperatures [16]. Extensive research has been carried out on the microstructure and properties of traditional Al−Cu alloys, providing a valuable foundation for the development of WAAM Al−Cu alloys.

Generally, the nanoscale θ' precipitate in the aged Al−Cu alloys exhibits excellent coarsening resistance up to 250 °C [17]. Nevertheless, the metastable θ' precipitate rapidly transforms to equilibrium θ precipitate at higher temperatures. Research by ZHAO et al [18] indicated that the majority of the θ' precipitate in AlSiCuMg alloy dissolved into the Al matrix after heat exposure at 350 °C for 100 h. Since the θ' precipitate easily coarsens at elevated temperatures, micro-alloying is widely employed to improve thermal stability. BAHL et al [19] found that the volume fraction of θ' precipitate stabilized in the Al−Cu−Mn−Zr alloy after thermal exposure at 300 °C for 5000 h, due to the synergistic effect of Mn and Zr. They explained the precipitation strengthening using the Orowan mechanism and transformation strain. JIANG et al [20] discovered that adding Sc, Zr, and Mn to Al−Cu alloy could refine and stabilize the θ' precipitates, and the hardness remained stable even after thermal exposure at 280 °C for 24 h. LI et al [21] studied the effects of Mn and Zr micro-alloying on the high-temperature strength of Al−11.5Si−Cu alloy during thermal exposure. They observed that adding Mn effectively inhibited the precipitate transformation of $\theta' \rightarrow \theta$, while Zr had the opposite effect.

ZL205A alloy is a typical cast Al−Cu alloy for its strength at room temperature, primarily due to precipitation hardening from nano-θ' precipitate. However, when used in the high-temperature environments (200−300 °C) like aerospace and automotive, the nano-precipitates formed during the aging process tend to coarsen, leading to a significant decrease in mechanical properties. Therefore, enhancing the high-temperature thermal resistance of Al−Cu alloys has become a major challenge. Previous research mainly concentrated on the as-cast ZL205A alloy, neglecting the exploration of WAAM-ZL205A alloy and its performance under thermal exposure [22,23]. In this study, the ZL205A alloy was fabricated using CMT-WAAM, and the effects of aging and thermal exposure on the microstructure and mechanical properties were investigated.

2 Experimental

2.1 Alloy preparation

ZL205A alloy wires with a diameter of 1.2 mm were prepared by casting, extrusion, and drawing. Inductively coupled plasma atomic emission spectroscopy (ICP-AES) was utilized to analyze the chemical composition of the wire and deposited alloy, and the results are given in Table 1. A necessary 2024-Al plate (250 mm × 100 mm × 10 mm) was selected as the substrate. Prior to deposition, the substrate was cleaned using alcohol to remove the oil and impurities.

Table 1 Chemical compositions of wire and deposited ZL205A alloy (wt.%)

Alloy	Cu	Mn	Zr	Ti	Cd	V	Al
Wire	4.97	0.40	0.20	0.23	0.16	0.11	Bal.
Deposited	4.73	0.41	0.20	0.24	0.12	0.11	Bal.

A ZL205A alloy (200 mm × 30 mm × 80 mm) was manufactured using a cold metal transfer advance (CMT-ADV) system. The system included a Lungo PNT 3.0 control system, a Fronius Transpulse Synergic 4000 CMT heat source system, an IRB4600-40/2.55 industrial robot, and a wire feeder. Table 2 shows the welding parameters of

Table 2 CMT-WAAM parameters for ZL205A alloy in present work

Parameter	U/V	I/A	v_{TS}/(m·s^{-1})	v_{WFS}/(m·min^{-1})	H_{Layer}/mm	t_{ID}/s	T_P/°C	R_{SG}/(L·min^{-1})	W_{SO}/mm
Value	13	210	0.02	5.6−6.5	2.2	60	160	25	8−12

welding voltage (U), arc current (I), travel speed (v_{TS}), wire feed speed (v_{WFS}), layer height (H_{Layer}), interlayer delay (t_{ID}), preheated temperature (T_P), shielding gas flow rate (R_{SG}), and the wire stick-out (W_{SO}). The welding process involved a continuous and serpentine scanning strategy, with pure argon (99.99%) used as the protective gas.

2.2 Heat treatment

Specimens were chosen from the middle layer of the WAAM-ZL205A alloy. A sketch illustrating the heat treatment process is shown in Fig. 1. The procedure involved quenching the alloy in water immediately after being held at 535 °C for 10 h, followed by aging at 175 °C for 0−48 h and then air cooling (T6). Another set of specimens was held at 175 °C for 10 h and then subjected to thermal exposure at 200, 250, and 300 °C for 0−720 h before being air cooled.

2.3 Characterization of microstructure and mechanical properties

The microstructure of the WAAM-ZL205A alloy was performed using scanning electron microscopy (SEM, TESCAN MIRA3), X-ray diffraction (XRD, Rigaku D/max), and transmission electron microscopy (TEM, FEI Talos F200X). Samples for SEM and XRD measurements were prepared by wire cut electrical discharge machining (WEDM), followed by grinding with SiC papers and mechanical polishing. Notably, the samples were observed without the need for etching. The SEM observations were conducted using backscatter electron (BSE) diffraction. The XRD tests were carried out using Cu K_α radiation with a scanning speed of 5 (°)/min and a diffraction angle range of 10°−90°, and the precipitates were calibrated using an MDI-Jade 6.5 software. The TEM specimens with dimensions of 10 mm × 15 mm × 0.8 mm were thinned to 60 μm using metallographic abrasive paper, followed by punching discs with 3 mm in diameter and twin-jet electropolishing in an electrolyte of HNO_3 and CH_3OH (3:7 in volume ratio) at −25 °C and 14 V. TEM observations were carried out on an FEI Talos F200X instrument with mounted high-angle annular dark field (HAADF) detectors operated at 200 kV, focusing on the $\langle 100\rangle_{Al}$ crystal belt axis. The fast Fourier transformation (FFT) of high-resolution images was employed with Gatan Digital Micrograph software.

The hardness of the WAAM-ZL205A alloy was measured using a digital Brinell hardness tester with a load of 250 kg and a dwell time of 30 s. Before testing, the specimen surfaces were metallographically polished. The average hardness was determined based on a minimum of five indents. Tensile specimens of 60 mm in length and 2 mm in thickness were cut by WEDM, as shown in Fig. 1. Room-temperature tensile tests were conducted on an MTS−810 testing machine with a fixed rate of 2 mm/min. Three identical tensile specimens were prepared for testing, and the fracture morphologies were observed using SEM.

3 Results

3.1 Microstructural characteristics

3.1.1 SEM and XRD analysis results

Figure 2 shows the SEM microstructures of the WAAM-ZL205A alloy under various conditions. The white areas indicate precipitates, while the gray

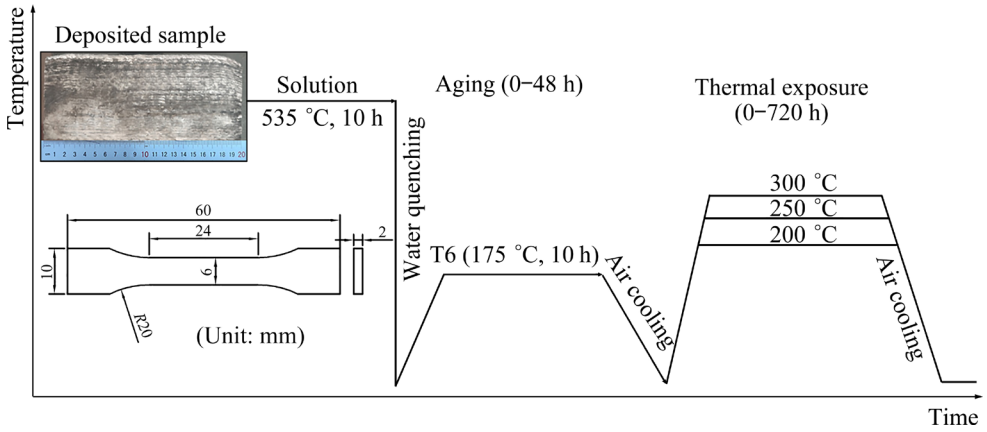

Fig. 1 Sketch of heat treatment procedure and tensile specimen of WAAM-ZL205A alloy

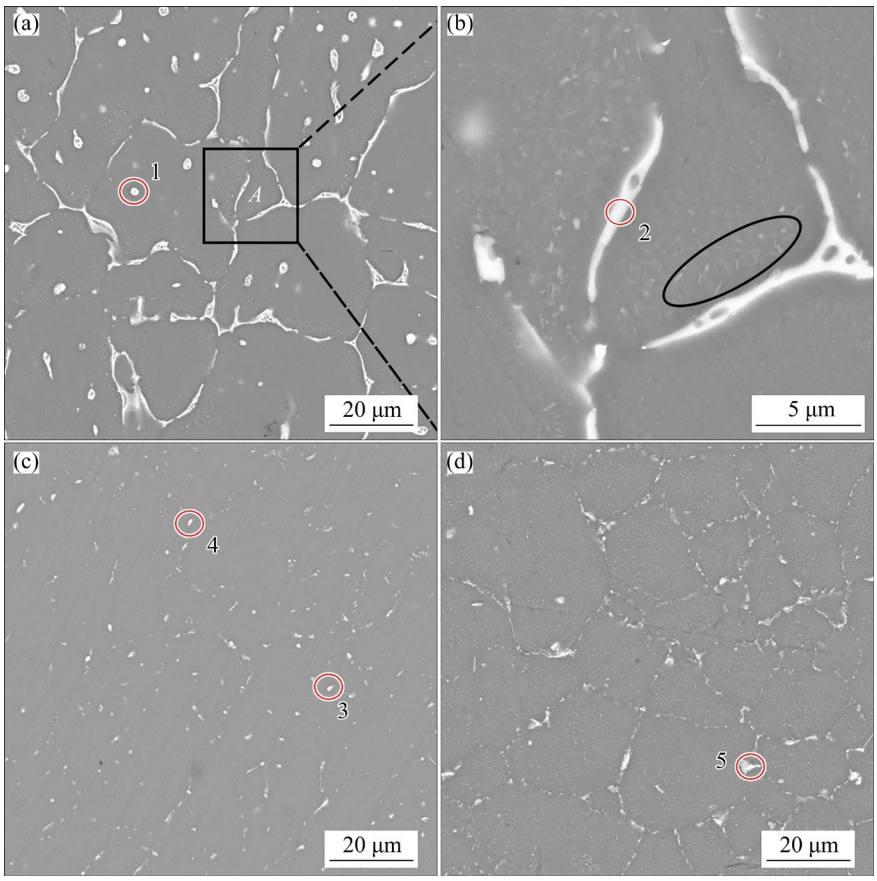

Fig. 2 SEM images of WAAM-ZL205A alloy: (a) Deposited; (b) Magnified image of Area *A* in (a); (c) T6-treated; (d) Thermally exposed at 300 °C for 24 h

area represents the matrix. In Fig. 2(a), a large number of irregular net-shape eutectic colonies (α-Al+θ-Al_2Cu) are visible, with most of them clustering along the grain boundary and some dispersed as independent particles within the grain. Figure 2(b) shows a lot of fine white needle-shaped secondary precipitates surrounding the eutectic, highlighted by a black ellipse. After T6 treatment, the volume fraction of these white secondary precipitates notably decreases, as shown in Fig. 2(c). This reduction is attributed to the dissolution of larger white secondary phases at the grain boundaries and within the grains during the solid solution treatment stage. The disappeared eutectics dissolve into the Al matrix to form a supersaturated solid solution, thus enhancing solid solution strengthening and providing solute atoms for subsequent aging precipitation. After thermal exposure at 300 °C for 24 h, there is a significant increase in the volume fraction of white secondary precipitates compared to the T6 treatment, and they are distributed discontinuously along the grain boundary (Fig. 2(d)).

EDS analysis was performed on the secondary precipitates located at the grain boundary and within the grain, identified as Points 1−5 in Fig. 2, and the results are detailed in Table 3. When comparing the chemical compositions of Points 1 and 2, it is observed that the grain boundary eutectic contains slightly higher levels of Mn than the inner grain eutectic, but the content of other elements is very similar. The EDS results of the T6-treated alloy reveal that Zr content in the residual white secondary precipitate increases from 0.05 at.% to 2.23 at.%, while Cu content decreases

Table 3 Chemical compositions of secondary precipitates in Fig. 2 (at.%) by EDS

Point	Al	Cu	Mn	Zr	Cd	Ti	V
1	86.06	12.77	0.89	0.05	0.15	0.01	0.06
2	85.40	12.38	1.97	0.04	0.03	0.01	0.17
3	88.93	6.68	1.79	2.23	0.04	0.07	0.08
4	82.05	4.77	2.55	0.40	0.00	0.04	0.19
5	86.92	7.32	5.03	0.15	0.10	0.03	0.46

by around 50%. After thermal exposure at 300 °C for 24 h, Cu content in the coarse white secondary precipitate increases, and Mn content is abnormally high.

Figure 3 shows the distribution of Cu, Mn, and Zr in the deposited, T6-treated, and thermally exposed alloys, respectively. In the deposited state, a large amount of Cu is found in θ precipitates at the grain boundary, with only a small amount is uniformly distributed within the grain. A small amount of Mn is also present in the θ precipitate, while the rest is evenly spread in the Al matrix. Following T6 treatment, Cu and Mn are distributed evenly due to the dissolution of the eutectic during the solid solution, and nanoscale θ'' and θ' phases precipitate during aging process. After thermal exposure at 300 °C for 24 h, it can be seen from Figs. 3(j, k) that Cu and Mn are observed to re-enrich as clusters at the grain boundary. As depicted in Figs. 3(d, h, l), Zr does not show significant segregation in the Al matrix after either T6 treatment or thermal exposure.

XRD patterns of the deposited, T6-treated, and thermally exposed WAAM-ZL205A alloys are shown in Fig. 4. Initially, the deposited alloy is primarily composed of α-Al and θ precipitate. After T6 treatment and subsequent thermal exposure, the diffraction peaks associated with the θ precipitate disappear, indicating that most of them dissolve into the Al matrix during the solid solution treatment. The thermally exposed alloy shows the presence of the Al_7Cu_2Fe (β-Fe) phase, and this phase is formed during the rapid solidification of the alloy at the eutectic stage of 530−540 °C [24].

3.1.2 TEM observation

The TEM microstructures of the deposited WAAM-ZL205A alloy are shown in Fig. 5. The bright-field image reveals that the net-shaped and short rod-shaped θ precipitate is distributed along the grain boundary and within the grain, respectively. Additionally, the low-density θ' precipitates are observed within the grain. The selected area electron diffraction (SAED) pattern along the [100] axis is displayed in Fig. 5(b), where the primary spots correspond to the α-Al phase, and the smaller spots highlighted by yellow circles are identified as

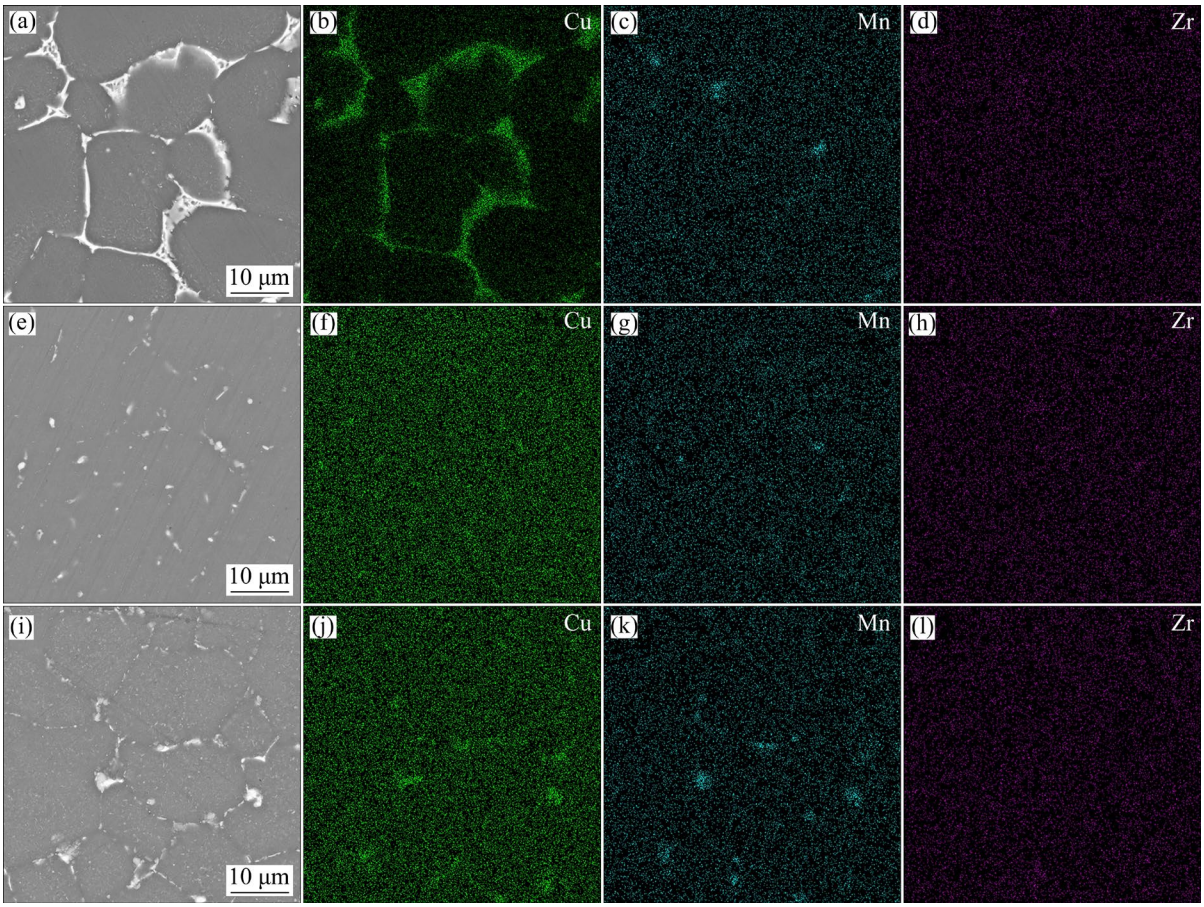

Fig. 3 SEM images and elemental distribution for deposited (a−d), T6-treated (e−h), and thermally exposed (i−l) WAAM-ZL205A alloys: (a, e, i) SEM images; (b, f, j) Distribution of Cu; (c, g, k) Distribution of Mn; (d, h, l) Distribution of Zr

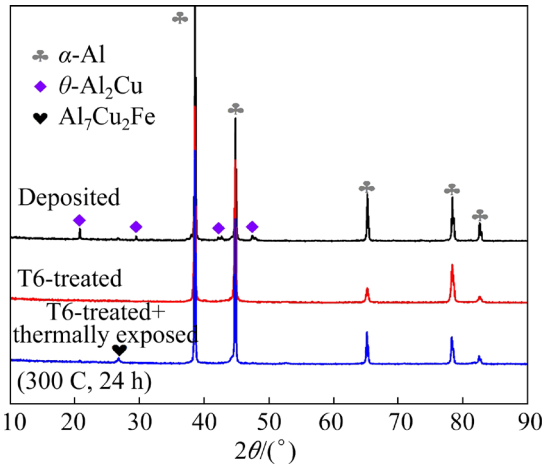

Fig. 4 XRD patterns of WAAM-ZL205A alloy under different conditions

θ' precipitate [25]. A high-resolution image of the θ' precipitate, approximately 18 nm in thickness, is shown in Fig. 5(c), displaying a semi-coherent relationship with the α-Al matrix. The nano-precipitate is determined to be θ'-Al_2Cu according to the associated FFT pattern.

HAADF-STEM images of nano-precipitates in the deposited alloy are shown in Figs. 5(e−h). The STEM-EDS results indicate that Cu is predominantly concentrated in the disc and needle-shaped secondary precipitates. The disc-shaped secondary precipitate corresponds to the θ phase and is distributed within the grain, as displayed in Fig. 2(a). Cd is primarily segregated in the dot-shaped secondary precipitate, which surrounds the rim of θ and θ' precipitates. Additionally, the Cd-containing precipitate is also embedded in the head of the θ' precipitate in the form of a hexagonal cube, as shown in Fig. 5(g).

The TEM microstructures of the T6-treated alloy are displayed in Fig. 6. In the SAED pattern, a discontinuous white streak marked by a red arrow is identified as θ'' precipitates, as shown in Fig. 6(a). Following the T6 treatment, it can be observed in Figs. 6(b, c) that the coarse net-shaped white θ precipitates distributed along the grain boundary almost vanish, and a large amount of θ'' and θ' phases precipitate within the grain. However, some residual θ precipitate and polygonal T-phase ($Al_{20}Cu_2Mn_3$) are also observed within the grains. The T-phase appears rod-shaped and has a polygonal “apple” shape on the cross-section, exhibiting higher thermal stability compared to the θ precipitate [26,27]. The volume fraction of the needle-shaped θ' precipitate in the alloy has notably increased compared to the initial deposited alloy. Additionally, the θ'' and θ' phases in the alloy precipitate during the aging process rather than directly transforming from the θ' precipitates in the deposited alloy. According to the Al−Cu alloy phase diagram [28], the θ' phase precipitates at 100−400 °C. Consequently, the θ' phase in the deposited alloy dissolves during the solution treatment at 535 °C.

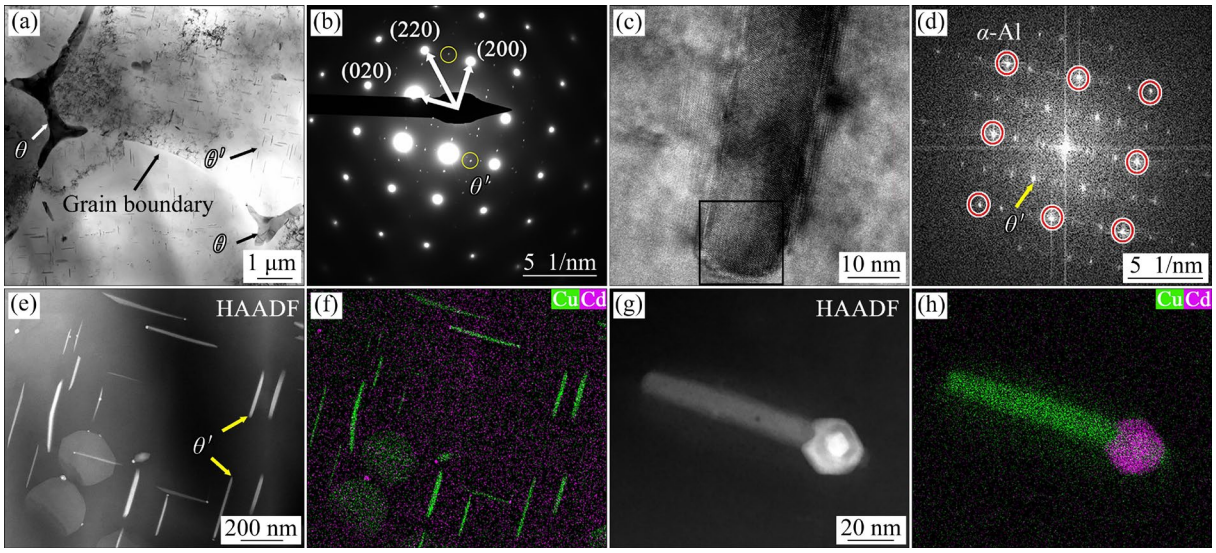

Fig. 5 TEM images of deposited alloy: (a, b) Bright-field image and corresponding SAED pattern, respectively; (c) High-resolution image of θ' precipitate; (d) FFT patterns of area indicated by black rectangle in (c); HAADF-STEM images (e, g) and nanoscale EDS mappings (f, h) of Cu and Cd

HAADF-STEM was used to determine chemical composition of the nanoscale secondary precipitates, and the results are shown in Fig. 7. In Fig. 7(a), it is evident that the T6-treated alloy contains a large amount of θ'' and θ' precipitates. The residual θ precipitate, approximately 500 nm, is dispersed within the grain. The net-shaped θ precipitate at the grain boundary dissolves into the Al matrix during the solid solution process, leading to the precipitation of the θ' phase in the aging process, forming the precipitate-free zones marked by the blue dashed lines. Additionally, Fig. 7(d) demonstrates that the Cd-containing precipitate plays a role in the formation of the θ' precipitate. The EDS mappings reveal that Cu and Cd are primarily present in the respective secondary precipitates, while Mn is evenly distributed throughout the Al matrix.

The TEM microstructures of the precipitates in the alloy after thermal exposure at 300 °C for 24 h are shown in Fig. 8. In Fig. 8(a), it is evident that the secondary precipitate at the grain boundary has grown further and some of the θ' precipitate has transformed into the θ precipitate compared to the T6-treated alloy. Since the time required for Cu atoms to diffuse from the grain boundary into the grain, the θ' precipitate within the grain does not transform into the θ precipitate. The undissolved θ precipitate is also observed, as shown in Figs. 8(b, c). Meanwhile, the θ' and Cd-containing

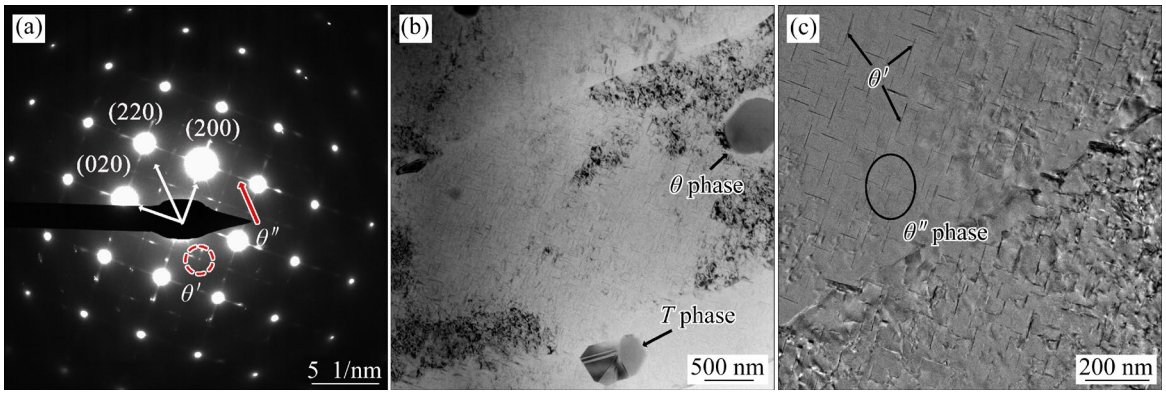

Fig. 6 TEM images of T6-treated alloy: (a) SAED pattern; (b, c) Bright-field images

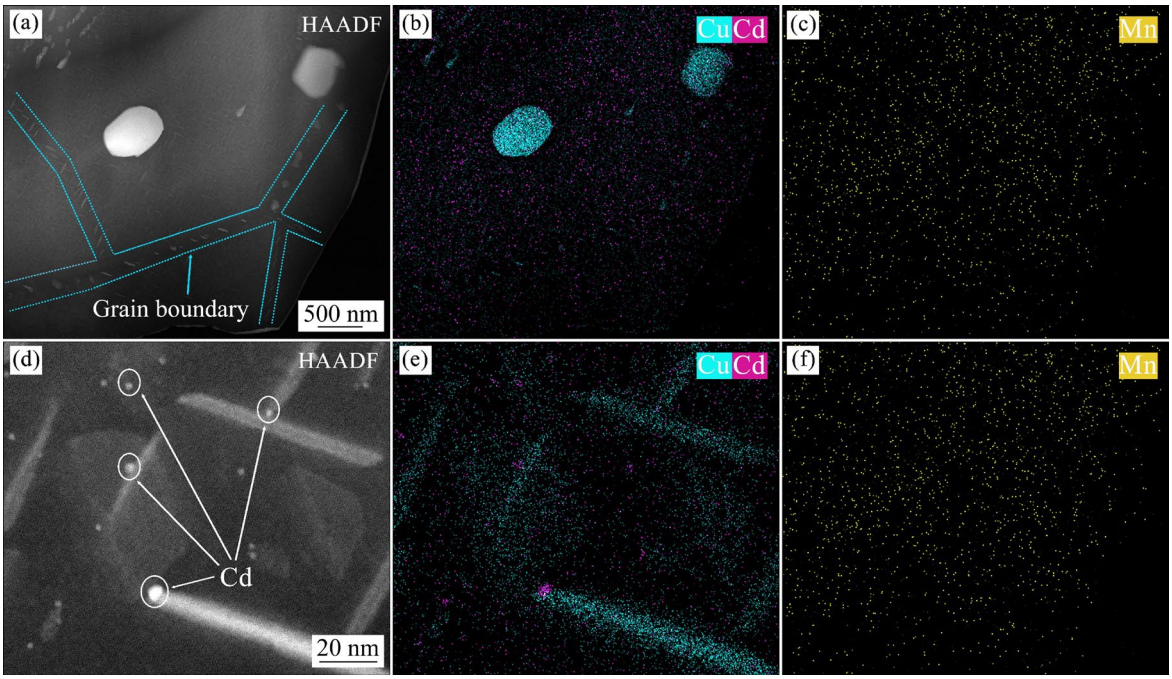

Fig. 7 HAADF-STEM images of T6-treated alloy: (a, d) HAADF images; (b, e) Distribution of Cu and Cd; (c, f) Distribution of Mn

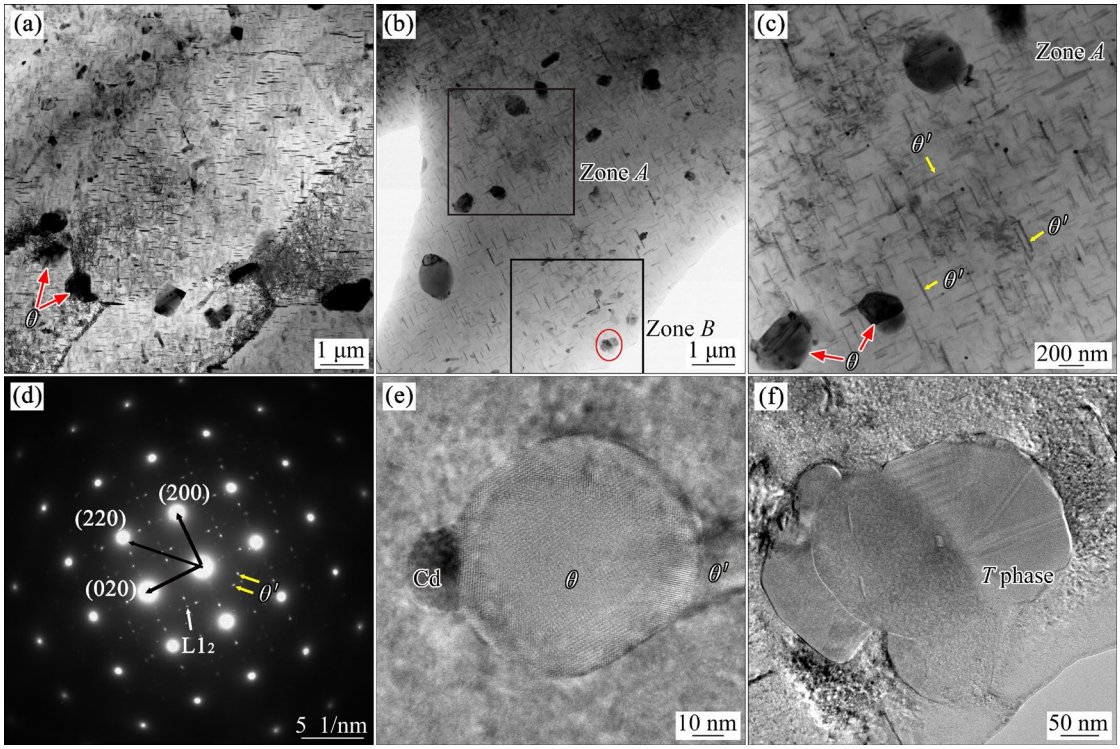

Fig. 8 TEM images of alloy thermally exposed at 300 °C for 24 h: (a−c) Bright-field images; (d) SAED pattern; (e, f) High-resolution images

precipitates in the alloy have significantly coarsen. The corresponding SAED pattern in Fig. 8(d) indicates that the discontinuous white streak disappears, confirming that the θ'' phase transforms into the θ' phases following thermal exposure treatment.

Figure 8(e) shows a high-resolution image of the θ precipitate with a diameter of approximately 70 nm. Adjacent to it on the left and right sides there exist the Cd-containing precipitate and θ' precipitate, respectively. This observation suggests that the Cd-containing precipitate facilitates the transition from the θ' precipitate to the θ precipitate. Additionally, Fig. 8(f) displays a high-resolution image of the T-phase ($Al_{20}Cu_2Mn_3$).

Figure 9(a) shows the HAADF-STEM microstructure of Zone B in Fig. 8(b). Figures 9(b−f) exhibit the elemental distributions of Al, Cu, Mn, Cd and Zr, respectively. The transformation from θ' precipitate to θ precipitate is evident. Cu and Mn are segregated in the secondary precipitates, aligning with the SEM microstructure in Fig. 3. The EDS mappings of Cu and Mn in Figs. 9(c, d) reveal that the left section of the T-phase contains Al and Cu, while the right part with elongated stripes consists of Mn and a small quantity of Cu.

In addition, the Cd-containing precipitate is coarsened significantly compared to the T6-treated alloy. Figure 9(f) illustrates the even distribution of Zr within the Al matrix. The presence of the $L1_2$-Al_3Zr precipitates is verified by the diffraction spots indicated by the white arrow in Fig. 8(d) [17].

Bright-field images of the precipitates under various conditions are displayed in Fig. 10, and length size distributions of the θ'' and θ' precipitates are given in Fig. 11. In Figs. 10(a) and 11(a), it is evident that the average length size of the coarsen θ' precipitate in the deposited alloy reaches 270.1 nm, with a relatively low number fraction. Following the T6 treatment, finer θ'' and θ' precipitates are observed within the Al matrix. Figures 10(b) and 11(b) show that the average length size of the precipitate decreases to 49.4 nm, with a significant increase in number fraction. Notably, the average length size of the precipitates gradually increases with higher thermal exposure temperature. Figures 11(c−e) demonstrate that after thermal exposure at 200, 250, and 300 °C for 24 h, the average length sizes of the precipitates are 88.4, 145.7, and 197.3 nm, respectively. At 200 °C, the transformation of θ' precipitates into θ precipitates has not occurred, the number fraction of precipitates

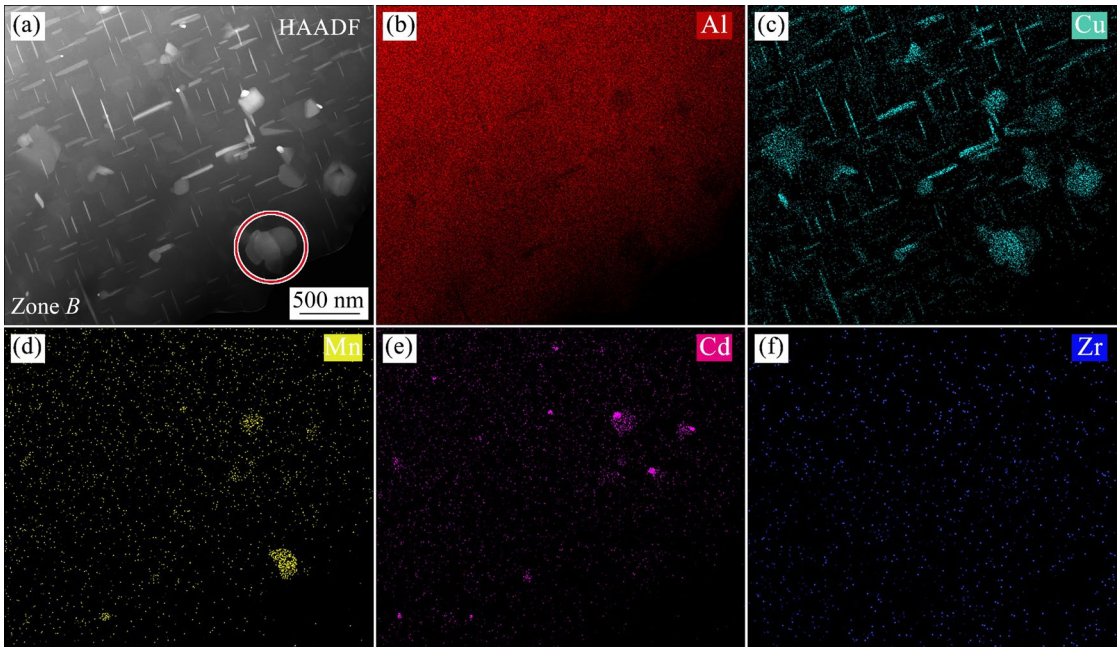

Fig. 9 HAADF-STEM microstructure and EDS mappings of Zone *B* in Fig. 8(b): (a) HAADF image; (b−f) Distribution of Al, Cu, Mn, Cd and Zr, respectively

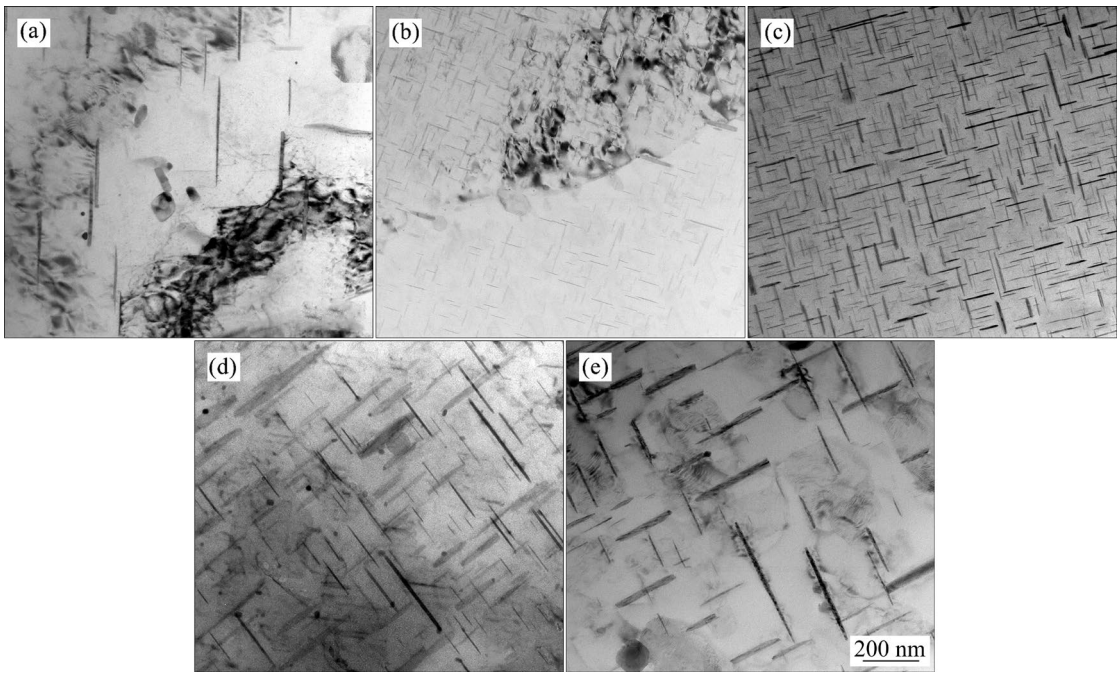

Fig. 10 Bright-field images of precipitates under different conditions: (a) As-deposited; (b) T6-treated; (c) Thermally exposed at 200 °C for 24 h; (d) Thermally exposed at 250 °C for 24 h; (e) Thermally exposed at 300 °C for 24 h

initially rises. The supersaturated Cu in theory contributes to further increasing the θ' phase number fraction, eventually reaching a metastable equilibrium value. After thermal exposure at 250 °C for 24 h, part of θ' precipitates begin to transform to θ precipitates. Therefore, the number fraction of the precipitates decreases, as displayed in Figs. 10(c−e).

3.2 Mechanical properties

3.2.1 Hardness

The hardness curve of the deposited alloy aged at 175 °C is shown in Fig. 12(a). The hardness of the deposited alloy is HB 79.7. It is observed that the hardness increases rapidly as the GP zone forms at the initial stage. After 10 h of aging time, the alloy reaches its peak hardness of HB 142.5 due to

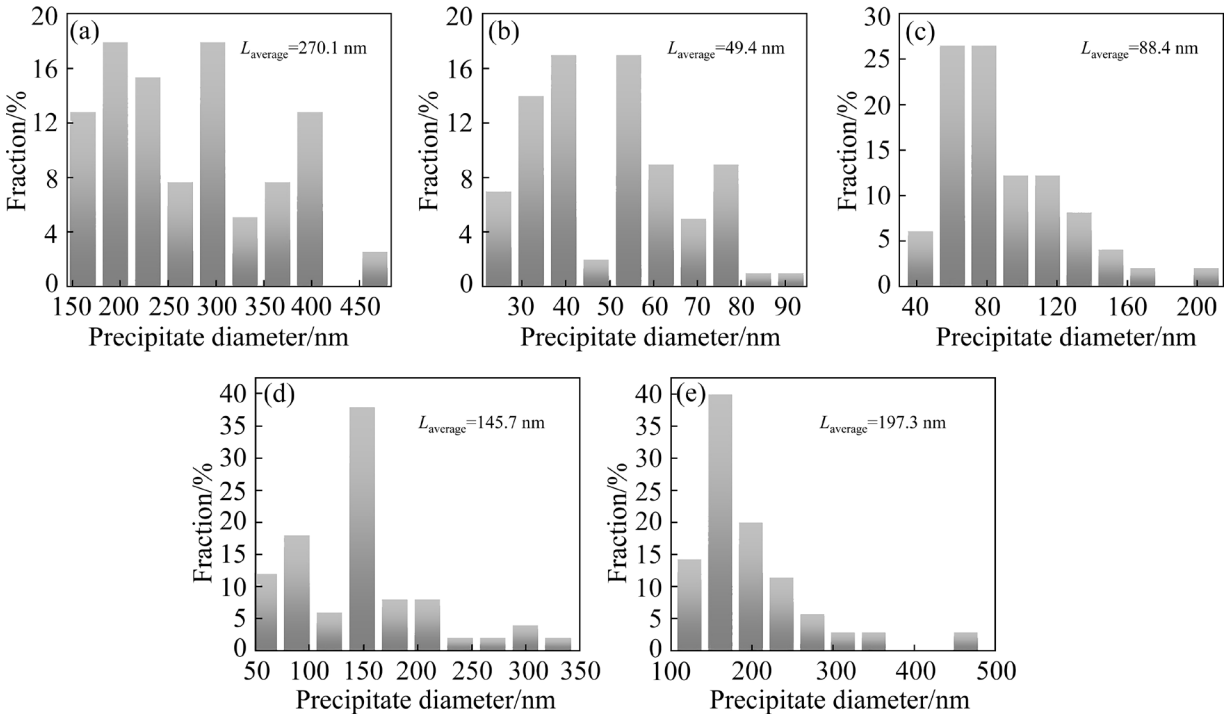

Fig. 11 Length size distribution of precipitates under different conditions: (a) Deposited; (b) T6-treated; (c) Thermally exposed at 200 °C for 24 h; (d) Thermally exposed at 250 °C for 24 h; (e) Thermally exposed at 300 °C for 24 h

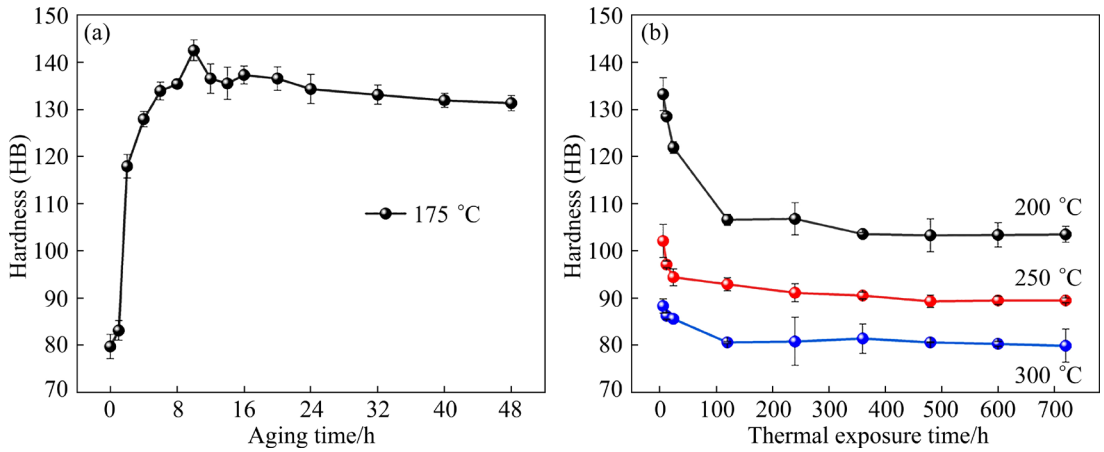

Fig. 12 Hardness variation curves of WAAM-ZL205A alloy under different conditions: (a) Aged at 175 °C; (b) Thermally exposed at 200, 250, and 300 °C for different time

the precipitation of θ'' and θ' phases. Even after 48 h of aging, the hardness only decreases by 7.7%, indicating that the WAAM-ZL205A alloy possesses strong resistance to over-aging.

Figure 12(b) demonstrates the hardness curves of the T6-treated alloy after thermal exposure at three different temperatures. It is seen that there is a notable decrease in the hardness under the three thermal exposure temperatures of 200, 250, and 300 °C at the initial stage. After 24 h, the hardness decreases to HB 121.9, HB 94.4, and HB 85.6, respectively. As the thermal exposure time extends to 120 h, the hardness further decreases to HB 103.6, HB 91.1, and HB 80.6, a decrease of 27.3%, 36.1%, and 43.4%, respectively, and then stabilizes. These findings indicate that the WAAM-ZL205A alloy remains quite stable at 250 °C. However, thermal exposure at 300 °C results in hardness levels returning to that of pre-T6 treatment. This suggests that the higher the thermal exposure temperature, the greater the reduction in hardness and the shorter time to reach stability.

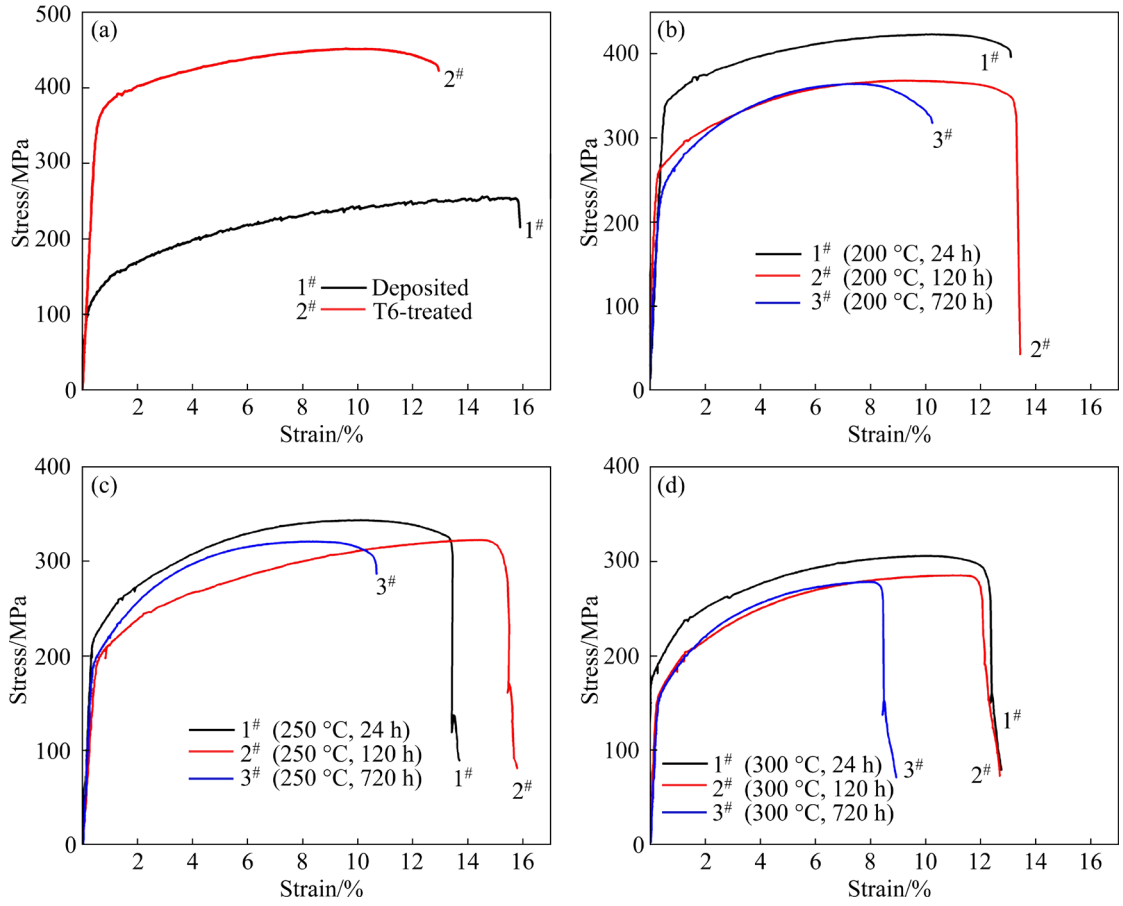

Fig. 13 Stress−strain curves of WAAM-ZL205A alloy under different conditions: (a) Deposited and T6-treated; (b−d) Thermally exposed at 200, 250, and 300 °C for different time, respectively

3.2.2 Tensile properties

Figure 13 shows tensile stress−strain curves of the alloys subjected to different treatments, with corresponding tensile properties detailed in Table 4. The T6-treated alloy exhibits significant enhancement in yield strength (YS) and ultimate tensile strength (UTS) compared to the deposited alloy, reaching 366.9 and 452.1 MPa, respectively. This improvement is primarily attributed to the strengthening effect of numerous fine θ'' and θ' precipitates, as observed in the TEM microstructure in Fig. 6. The data in Table 4 indicate that the variation of the YS and UTS with the extension of thermal exposure time is similar to that of hardness.

After thermal exposure at 200, 250, and 300 °C for 24 h, the YS decreases to 347.5, 225.8, and 188.9 MPa, a reduction of 5.3%, 38.5%, and 48.5%, respectively. With a longer thermal exposure time of 120 h, the YS further decreases by 27.8%, 43.3%, and 54.6%, respectively. When the time reaches 720 h, there is no significant decrease in the YS and UTS. Additionally, at higher exposure temperatures, the decrease in strength is less pronounced when extending the time from 120 to 720 h. The elongation (El) initially increases and

Table 4 Tensile properties of WAAM-ZL205A alloy under different conditions

Condition	YS/MPa	UTS/MPa	El/%
Deposited	133.0±2.9	256.1±2.7	15.9±0.22
T6-treated	366.9±0.5	452.1±4.9	12.9±0.19
TE (200 °C, 24 h)	347.5±1.7	423.6±5.1	13.1±0.11
TE (200 °C, 120 h)	264.8±2.1	368.6±3.8	13.4±0.12
TE (200 °C, 720 h)	242.8±3.1	364.5±4.1	10.3±0.14
TE (250 °C, 24 h)	225.8±3.3	353.7±3.2	13.9±0.17
TE (250 °C, 120 h)	207.9±1.7	322.7±4.8	15.8±0.12
TE (250 °C, 720 h)	200.7±2.2	321.2±5.2	10.7±0.17
TE (300 °C, 24 h)	188.9±1.9	305.9±3.4	12.8±0.16
TE (300 °C, 120 h)	166.4±2.3	285.3±4.2	12.6±0.21
TE (300 °C, 720 h)	165.1±1.6	278.5±4.7	8.9±0.11

TE: Thermally exposed

then decreases rapidly with longer thermal exposure at 200 and 250 °C, while it continuously decreases at 300 °C. The alloy matrix is softer than the precipitated phase, leading to inconsistent deformation under tensile stress. Therefore, the plasticity of the alloy is reduced due to the coarsening or the transformation of θ' precipitates after thermal exposure at 300 °C.

Tensile properties of Al−Cu alloys in the literatures are listed in Table 5. In contrast, Al−Cu alloys manufactured by other WAAM processes cannot obtain high strength and elongation after T6 treatment. The WAAM-ZL205A alloy demonstrates a marked improvement in YS and UTS compared to traditional casting alloy and comparable to those of the deformed alloys.

Table 5 Yield strengths of Al−Cu alloy in literatures

Alloy	YS/MPa	Ref.
T6-2219-WAAM	303±5	[16]
T6-2024-WAAM	374	[29]
T6-Al−5Cu−0.2Mn−0.2Zr (As-cast)	292.5±15.8	[25]
T6-Al−4Cu−0.05Sn (200 °C, 168 h)	174±1.6	[30]
T6-Al−6.7Cu−0.45Mn (300 °C, 5000 h)	194	[19]
T7-Al−4.74Cu−0.13Mg (300 °C, 100 h)	142	[31]
T7-Al−4.7Cu−0.35Mn−0.15Zr (300 °C, 100 h)	165	[17]
T6-Al−5Cu−Ni−Mn−Zr (300 °C, 100 h)	105	[32]

3.2.3 Fracture morphologies

The tensile fracture morphologies of the specimens following various treatments are shown in Fig. 14. All specimens have visible micro-pores, marked by black ellipses. The majority of these micro-pores are hydrogen pores generated during the WAAM process, which diminish the stressed area and destroy the grain boundary consistency [33]. These micro-pores act as crack-initiating points and accelerate the fracture during the tensile test, thus reducing the mechanical properties of the alloy. Typical intergranular fractures and tiny dimples are observed in the specimens before and after T6 treatment, as shown in Figs. 14(a) and (b). Furthermore, the T6-treated alloy displays no secondary precipitates at the bottom of the dimples, and the number of dimples on the fracture surface is significantly reduced, consistent with the decrease in plasticity.

The thermal exposure of the alloy can be considered an over-aging process. Thermal exposure at 200 °C for 24 h shows no significant difference in fracture morphology compared to the T6-treatment. However, dimples increase notably after thermal exposure at 250 °C for the same duration. The weak point of the T6-treated alloy is the grain boundaries, but locations at the grain

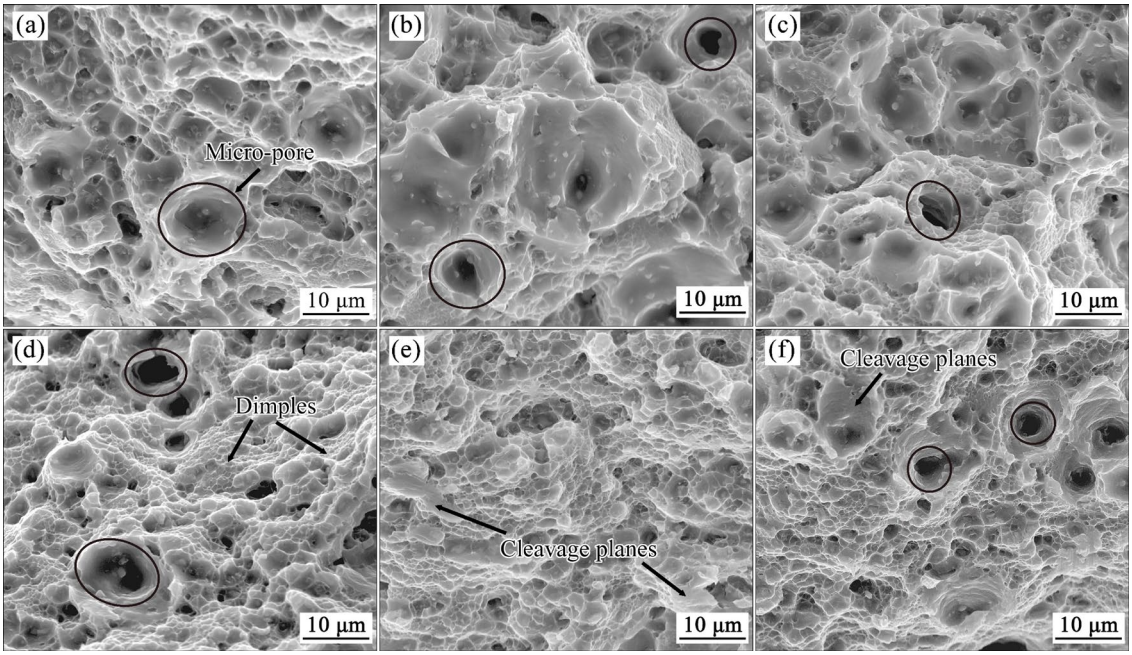

Fig. 14 Tensile fracture morphologies of WAAM-ZL205A alloy under different conditions: (a) Deposited; (b) T6-treated; (c−e) Thermally exposed at 200, 250, and 300 °C for 24 h, respectively; (f) Thermally exposed at 300 °C for 720 h

boundary and within the grains become the weak points due to the decrease in the density of precipitates after thermal exposure. This weakening within the grains can relieve stress concentration at the grain boundary, thereby enhancing the ductility of the alloy. After thermal exposure at 300 °C, obvious deformation is observed on the fracture surface, with a mix of cleavage planes and a small number of dimples, indicating a combination of ductile and brittle fractures. Consequently, the plasticity of the alloy decreases after thermal exposure at 300 °C.

4 Discussion

4.1 Microstructural evolution

The deposited ZL205A alloy mainly consists of α-Al phase, θ-Al_2Cu eutectic, and θ' precipitate, as shown in Figs. 2(a) and (b). The majority of the θ eutectics are distributed along the grain boundaries in a network pattern, with a few present within the grains in a disc-shaped form. The XRD patterns (Fig. 4) and TEM microstructure (Fig. 5(a)) confirm the presence of θ precipitate in the deposited alloy. Similar to other WAAM Al−Cu alloys, the α-Al phase first forms at the initial stage of the cooling process, followed by precipitation of the θ phase when the Cu concentration in the melt and temperature reach the eutectic point.

The θ' phase mainly forms around the net-shaped eutectics during the WAAM process, as shown in Figs. 2(b) and 5(e). The unique thermal cycle of the WAAM encourages the precipitation of θ' phase because the alloy deposited subsequently continuously heats the previously deposited alloy. In WAAM, the spherical θ''-Al_3Cu phase initially precipitates in the Cu-rich regions (around the eutectics) and then clusters to minimize the surface energy due to the thermal effect [34]. As the sampling in this study was in the middle of the deposited alloy, the prolonged thermal cycling causes the θ'' precipitate to coarsen and transform into the θ' precipitate. It is noted that only the θ' precipitate is observed in the deposited alloy, with no coarsened θ'' precipitate present. Additionally, Cd is mainly distributed as a dot-shaped secondary precipitate at the edge of θ and θ' precipitates, as shown in Figs. 5(e−h). DONG et al [35] reported that Cd had a high vacancy binding energy, and Cd-vacancy clusters provided numerous nucleation sites, thus reducing the nucleation energy of θ' precipitates. Besides, Cd contributes to the precipitation of θ' phase during the subsequent T6 treatment and the transformation of θ' to θ phase during thermal exposure. Therefore, Cd also plays a crucial role in improving the mechanical properties of Al−Cu alloys [36].

After T6 treatment, the majority of the θ-Al_2Cu eutectics located at the grain boundaries and within the grains dissolve into the Al matrix, as shown in Fig. 2(c). However, a few remaining white secondary precipitates are observed within the grain. The EDS results (Table 3) reveal that these secondary precipitates are primarily Zr-containing precipitates. This observation indicates that the Zr-containing precipitate possesses a high melting point and is resistant to dissolve even at a solid solution temperature of 535 °C. In addition, a significant amount of θ' and θ'' precipitates at the grain boundaries and within the grains are observed in Figs. 5 and 6. The size of the θ' precipitates at the grain boundaries is notably larger than that within the grains, indicating that the precipitates tend to nucleate preferentially in the Cu-rich area of the grain boundaries. It is notable that the θ' precipitate in the T6-treated alloy differs from that in the deposited alloy. Referring to the Al−Cu binary diagram [37], as the aging temperature increases (below 250 °C), the precipitation sequence of Al−5Cu alloy is GP zone → θ'' → θ'. Consequently, when the solid solution temperature is 535 °C, the primary θ' precipitate in the deposited alloy will dissolve into the Al matrix together with the θ-Al_2Cu eutectic.

After thermal exposure at 300 °C for 24 h, the T6-treated alloy exhibits further growth of the θ' precipitate both at the grain boundary and within the grain. Some of the θ' precipitates at the grain boundary transform into θ precipitates, as shown in Figs. 2(d) and 8(a). The segregation of Cu and Mn at the grain boundary contributes to transforming from θ' to θ precipitate. Previous research indicated that Mn tended to segregate at the interface of θ' precipitate during thermal exposure, leading to a reduction in interfacial energy and an enhancement in precipitate stability [38]. In addition, Zr is still distributed uniformly in the Al matrix even after thermal exposure. Studies have reported that Zr micro-alloying in Al−Cu alloys resulted in the formation of a small quantity of nano-Al_3Zr particles, which

played a critical role in improving the room temperature strength and stabilizing the metastable θ' precipitate at elevated temperatures [39,40]. The SAED pattern also demonstrates the presence of $L1_2$-Al_3Zr precipitate, as shown in Fig. 8(d).

Most of evolution in microstructure and properties occurs within the first 120 h, as indicated by the precipitate transformation (Fig. 8), hardness variation (Fig. 12), and mechanical properties variation (Fig. 13). The temperature-dependent phase stability leads to the initial evolution of microstructure. Since the thermal exposure temperature is 125 °C higher than the aging temperature, the thermodynamic stability of the θ' precipitate decreases during the thermal exposure, resulting in a slight reduction in the number density of the θ' precipitates. Consequently, the mechanical properties of the alloy regress to their pre-T6 treatment levels. After the initial evolution exceeds 120 h, the θ' precipitate stabilizes, leading to stabilization in mechanical properties as well.

4.2 Strengthening behavior

In Al−Cu alloys, the θ' precipitate coarsens with increasing heat treatment time and transforms into θ precipitate at high temperatures. After thermal exposure at 200, 250, and 300 °C, the average length size of the θ' precipitate increases by 78.9%, 213.2%, and 299.4%, respectively, as shown in Figs. 10 and 11. The thermo-dynamically driven coarsening of precipitates can be explained by the LSW relationship in Eq. (1) [19]:

$$\overline{r}^3 - r_0^3 = \frac{8}{9}\frac{\gamma D c_0 V_m^2}{RT}(t) \tag{1}$$

where $\overline{r}$ is the equivalent radius at given time t, r_0 is the equivalent radius of θ' and θ'' phase in the T6-treated alloy, γ is the interfacial energy, D is the diffusion coefficient of Cu at temperature T, c_0 is the equilibrium concentration of Cu, V_m is the molar volume of the precipitate, and R is the molar gas constant. It is seen that the lower interfacial energy upon segregation and the lower diffusivity of Cu at elevated temperatures are beneficial to decreasing the coarsening rate of the precipitates.

As mentioned, Zr does not undergo any significant transformation during aging and thermal exposure. This suggests that the strengthening effect of Zr is identical after different heat treatments. Therefore, only Orowan strengthening mechanism of the θ' precipitate is considered. After thermal exposure at 300 °C for 720 h, the θ' precipitate loses its strengthening effect, leaving only the solid solution strengthening ($\Delta\sigma_{ss}$) of Cu and Mn effective in the alloy. The calculated results show that the contribution of solid solution strengthening to YS is 32.1 MPa ($\Delta\sigma_{ss}=YS_{720\ h}-YS_{deposited}$). The contribution of Orowan strengthening of θ' precipitates ($\Delta\sigma_{os}$) to YS is calculated by Eq. (2) [31]:

$$\Delta\sigma_{os} = \frac{MGb}{2\pi\sqrt{1-\nu}}\left(\frac{1}{1.23\frac{1.030}{\sqrt{N_v d_p}} - \frac{\pi d_p}{8} - 1.061 t_p}\right) \cdot \ln\left(\frac{0.981\sqrt{d_p t_p}}{b}\right) \tag{2}$$

where M is the Taylor factor (3.06 for poly-crystalline fcc alloy), G is the shear modulus (28.0 GPa for α-Al matrix), ν is the Poisson ratio (0.33 for Al), b is the amplitude of the Burgers vector (0.286 nm for Al), N_v is the number density of precipitates, d_p is the true precipitate diameter, and t_p is the true precipitate thickness. Equation (2) states that the alloy strength is influenced by the number density and size of the θ' precipitate. A greater number density and smaller size of the precipitate result in a stronger alloy. Compared to the T6-treated alloy, the alloy after thermal exposure shows a gradual decrease in number density and an increase in the diameter of the θ' precipitate as the temperature rises, resulting in the weakening of its strengthening effect.

5 Conclusions

(1) The WAAM-ZL205A deposited alloy consists of α-Al, net-shaped θ-Al_2Cu eutectic and low-density θ' precipitate, with YS, UTS, and El of 133.0 MPa, 256.1 MPa and 15.9%, respectively.

(2) The average length size of the θ'' and θ' precipitates in the T6-treated alloy is 49.4 nm, leading to the increase of YS and UTS to 366.9 and 452.1 MPa, respectively, but a slight decrease of El to 12.9%.

(3) After thermal exposure at 300 °C for 24 h, the YS is reduced by 48.5% while El remains essentially unchanged. The microstructural evolution of the alloy mainly occurs within the initial 120 h,

after which the mechanical properties do not degrade with further thermal exposure.

(4) In the thermal exposure range of 200−300 °C, as the thermal exposure temperature rises, the average length size of the θ' precipitate increases while the number fraction decreases gradually. The T6-treated WAAM-ZL205A alloy can be applied in environments not exceeding 250 °C.

CRediT authorship contribution statement

Hai-jiang LIU: Validation, Formal analysis, Investigation, Resources, Writing – Original draft, Review & editing; **Yan FENG:** Validation, Investigation, Writing – Review & editing; **Chao-qun PENG:** Writing – Review; **Zhi-yong CAI:** Validation, Formal analysis, Writing – Review & editing, Funding acquisition, Resources; **Meng WANG:** Methodology, Conceptualization, Writing – Review & editing, Visualization, Supervision; **Zi-ming LI:** Conceptualization, Writing − Revision, Supervision; **Zhi-jie KANG:** Conceptualization, Supervision, Validation, Formal analysis; **Xiao-di ZHANG:** Methodology, Investigation, Supervision, Conceptualization.

Declaration of competing interest

The authors declare that they have no known competing financial interests or personal relationships that could have appeared to influence the work reported in this paper.

Ethical approval

The authors confirm that the manuscript is not under review or published elsewhere. The authors state that the research was conducted according to ethical standards. There is no ethical concern.

Acknowledgments

The authors are grateful for the financial support from the National Natural Science Foundation of China (No. 52274369), and the Science and Technology Program of Hunan Province, China (No. 2020GK2044).

References

[1] TONG Xin, WU Guo-hua, EASTON M A, SUN Ming, WANG Qi-man, ZHANG Liang. Microstructural evolution and strengthening mechanism of Mg−Y−RE−Zr alloy fabricated by quasi-directed energy deposition [J]. Additive Manufacturing, 2023, 67: 103487.

[2] SAMES W J, LIST F A, PANNALA S, DEHOFF R R, BABU S S. The metallurgy and processing science of metal additive manufacturing [J]. International Materials Reviews, 2016, 61: 315−360.

[3] KOTADIA H R, GIBBONS G, DAS A, HOWES P D. A review of laser powder bed fusion additive manufacturing of aluminium alloys: Microstructure and properties [J]. Additive Manufacturing, 2021, 46: 102155.

[4] PAOLINI A, KOLLMANNSBERGER S, RANK E. Additive manufacturing in construction: A review on processes, applications, and digital planning methods [J]. Additive Manufacturing, 2019, 30: 100894.

[5] MARTIN J H, YAHATA B D, HUNDLEY J M, MAYER J A, SCHAEDLER T A, POLLOCK T M. 3D printing of high-strength aluminium alloys [J]. Nature, 2017, 549: 365−369.

[6] ABOULKHAIR N T, SIMONELLI M, PARRY L, ASHCROFT L, TUCK C, HAGUE R. 3D printing of aluminium alloys: Additive manufacturing of aluminium alloys using selective laser melting [J]. Progress in Materials Science, 2019, 106: 100578.

[7] GENG Ru-wei, DU Jun, WEI Zheng-ying, MA Nin-shu. Multiscale modelling of microstructure, micro-segregation, and local mechanical properties of Al−Cu alloys in wire and arc additive manufacturing [J]. Additive Manufacturing, 2020, 36: 101735.

[8] WANG Xiao-long, WANG Ai-min, WANG Kai-xiang, LI Yue-bo. Process stability for GTAW-based additive manufacturing [J]. Rapid Prototyping Journal, 2019, 25: 809−819.

[9] ARTAZA T, SUÁREZ A, VEIGA F, BRACERAS I, TABERNERO I, LARRAÑAGA O, LAMIKIZ A. Wire arc additive manufacturing Ti_6Al_4V aeronautical parts using plasma arc welding: Analysis of heat-treatment processes in different atmospheres [J]. Journal of Materials Research and Technology, 2020, 9: 15454−15466.

[10] LI Sen, ZHANG Lin-jie, NING Jie, WANG Xiang, ZHANG Gui-feng, ZHANG Jian-xun, NA S J, FATEMEH B. Comparative study on the microstructures and properties of wire plus arc additively manufactured 5356 aluminium alloy with argon and nitrogen as the shielding gas [J]. Additive Manufacturing, 2020, 34: 101206.

[11] JANG J H, NAM D G, PARK Y H, PARK I M. Effect of solution treatment and artificial aging on microstructure and mechanical properties of Al−Cu alloy [J]. Transactions of Nonferrous Metals Society of China, 2013, 23: 631−635.

[12] BELOV N A, KOROTKOVA N O, AKOPYAN T K, PESIN A M. Phase composition and mechanical properties of Al−1.5%Cu−1.5%Mn−0.35%Zr(Fe,Si) wire alloy [J]. Journal of Alloys and Compounds, 2019, 782: 735−746.

[13] YANG C, ZHANG P, SHAO D, WANG R H, CAO L F, ZHANG J Y, LIU G, CHEN B A, SUN J. The influence of Sc solute partitioning on the microalloying effect and mechanical properties of Al−Cu alloys with minor Sc addition [J]. Acta Materialia, 2016, 119: 68−79.

[14] ELHADARI H A, PATEL H A, CHEN D L, KASPRZAK W. Tensile and fatigue properties of a cast aluminum alloy with

Ti, Zr and V additions [J]. Materials Science and Engineering: A, 2011, 528: 8128−8138.

[15] MA P P, LIU C H, WU C L, LIU L M, CHEN J H. Mechanical properties enhanced by deformation-modified precipitation of θ'-phase approximants in an Al−Cu alloy [J]. Materials Science and Engineering: A, 2016, 676: 138−145.

[16] ZHOU Ying-hui, LIN Xin, KANG Nan, HUANG Wei-dong, WANG Zhen-nan. Mechanical properties and precipitation behavior of the heat-treated wire + arc additively manufactured 2219 aluminum alloy [J]. Materials Characterization, 2021, 171: 110735.

[17] LI D, LIU K, RAKHMONOV J, CHEN X G. Enhanced thermal stability of precipitates and elevated-temperature properties via microalloying with transition metals (Zr, V and Sc) in Al−Cu 224 cast alloys [J]. Materials Science and Engineering: A, 2021, 827: 142090.

[18] ZHAO Bei-bei, YE Bing, WANG Li-yang, BAI Yang, YU Xin, WANG Qi-gui, YANG Wen-ying. Effect of ageing and thermal exposure on microstructure and mechanical properties of a HPDC Al−Si−Cu−Mg alloy [J]. Materials Science and Engineering: A, 2022, 849: 143463.

[19] BAHL S, XIONG L H, ALLARD L F, MICHI R A, POPLAWSKY J D, CHUANG A C, SINGH D, WATKINS T R, SHIN D, HAYNES J A, SHYAM A. Aging behavior and strengthening mechanisms of coarsening resistant metastable θ' precipitates in an Al−Cu alloy [J]. Materials & Design, 2021, 198: 109378.

[20] JIANG L, ROUXEL B, LANGAN T, DORIN T. Coupled segregation mechanisms of Sc, Zr and Mn at θ' interfaces enhances the strength and thermal stability of Al−Cu alloys [J]. Acta Materialia, 2021, 206: 116634.

[21] LI Guang-jing, LIAO Heng-cheng, ZHENG Ji-wei, CHEN Hao, LU Li-Zhen, YANG Lin-long, GUO Hui-ting. Micro-alloying effects of Mn and Zr on the evolution of ageing precipitates and high temperature strength of Al−11.5Si−4Cu alloy after a long-time heat exposure [J]. Materials Science and Engineering: A, 2021, 828: 142121.

[22] LUO Lei, XIA Hong-ying, LUO Liang-shun, SU Yan-qing, CAI Chao-jun, WANG Liang, GUO Jing-jie, FU Heng-zhi. Eliminating shrinkage defects and improving mechanical performance of large thin-walled ZL205A alloy castings by coupling travelling magnetic fields with sequential solidification [J]. Transactions of Nonferrous Metals Society of China, 2021, 31: 865-877.

[23] LI Bo, SHEN Yi-fu, HU Wei-ye. Casting defects induced fatigue damage in aircraft frames of ZL205A aluminum alloy—A failure analysis [J]. Materials & Design, 2011, 32: 2570−2582.

[24] LIU K, CAO X, CHEN X G. Solidification of iron-rich intermetallic phases in Al−4.5Cu−0.3Fe cast alloy [J]. Metallurgical and Materials Transactions A, 2011, 42: 2004−2016.

[25] SUN Teng-teng, GENG Ji-wei, BIAN Ze-yu, WU Yi, WANG Ming-liang, CHEN Dong, MA Nai-heng, WANG Hao-wei. Enhanced thermal stability and mechanical properties of high-temperature resistant Al−Cu alloy with Zr and Mn micro-alloying [J]. Transactions of Nonferrous Metals Society of China, 2022, 32: 64−78.

[26] DAR S M, LIAO Heng-cheng, XU Ai-qun. Effect of Cu and Mn content on solidification microstructure, T-phase formation and mechanical property of AlCuMn alloys [J]. Journal of Alloys and Compounds, 2019, 774: 758−767.

[27] WANG J, ZHANG B, HE Z B, WU B, MA X L. Atomic-scale mapping of twins and relevant defective structures in $Al_{20}Cu_2Mn_3$ decagonal approximant [J]. Philosophical Magazine, 2016, 96: 2457−2467.

[28] ZHOU Si-yu, WU Ke, YANG Guang, WU Bin, QIN Lan-yun, WU Hao, YANG Chao-yue. Microstructure and mechanical properties of wire arc additively manufactured 205A high strength aluminum alloy: The comparison of as-deposited and T6 heat-treated samples [J]. Materials Characterization, 2022, 189: 111990.

[29] QI Ze-wu, QI Bo-jin, CONG Bao-qiang, SUN Hong-ye, ZHAO Gang, DING Jia-luo. Microstructure and mechanical properties of wire + arc additively manufactured 2024 aluminum alloy components: As-deposited and post heat-treated [J]. Journal of Manufacturing Processes, 2019, 40: 27−36.

[30] NIE J F, MUDDLE B C. Strengthening of an Al–Cu–Sn alloy by deformation-resistant precipitate plates [J]. Acta Materialia, 2008, 56: 3490−3501.

[31] RAKHMONOV J, LIU K, PAN L, BRETON F, CHEN X G. Enhanced mechanical properties of high-temperature-resistant Al−Cu cast alloy by microalloying with Mg [J]. Journal of Alloys and Compounds, 2020, 827: 154305.

[32] SHYAM A, ROY S, SHIN D, POPLAWSKY J D, ALLARD L F, YAMAMOTO Y, MORRIS J R, MAZUMDER B, IDROBO J C, RODRIGUEZ A, WATKINS T R, HAYNES J A. Elevated temperature microstructural stability in cast AlCuMnZr alloys through solute segregation [J]. Materials Science and Engineering: A, 2019, 765: 138279.

[33] GU Jiang-long, GAO Min-jie, YANG Shou-liang, BAI Jing, DING Jia-luo, FANG Xue-wei. Pore formation and evolution in wire + arc additively manufactured 2319 Al alloy [J]. Additive Manufacturing, 2019, 30: 100900.

[34] WANG Zhen-nan, LIN Xin, WANG Li-lin, CAO Yang, ZHOU Ying-hui, HUANG Wei-dong. Microstructure evolution and mechanical properties of the wire + arc additive manufacturing Al−Cu alloy [J]. Additive Manufacturing, 2021, 47: 102298.

[35] DONG Ming-ye, ZHAO Yue, LI Quan, WANG Fu-de, WU Ai-ping. Effects of Cd addition in welding wires on microstructure and mechanical property of wire and arc additively manufactured Al−Cu alloy [J]. Transactions of Nonferrous Metals Society of China, 2022, 32: 750−764.

[36] SOFYAN B T, RAVIPRASAD K, RINGER S P. Effects of microalloying with Cd and Ag on the precipitation process of Al−4Cu−0.3Mg (wt.%) alloy at 200 °C [J]. Micron, 2001, 32: 851−856.

[37] WU Dong-jiang, LIU De-hua, NIU Fang-yong, MIAO Qiu-yu, ZHAO Kai, TANG Bo-kai, BI Gui-jun, MA Guang-yi. Al−Cu alloy fabricated by novel laser-tungsten

inert gas hybrid additive manufacturing [J]. Additive Manufacturing, 2020, 32: 100954.

[38] POPLAWSKY J D, MILLIGAN B K, ALLARD L F, SHIN D, SHOWER P, CHISHOLM M F, SHYAM A. The synergistic role of Mn and Zr/Ti in producing θ′/L12 co-precipitates in Al−Cu alloys [J]. Acta Materialia, 2020, 194: 577−586.

[39] DORIN T, RAMAJAYAM M, LAMB J, LANGAN T. Effect of Sc and Zr additions on the microstructure/strength of Al−Cu binary alloys [J]. Materials Science and Engineering: A, 2017, 707: 58−64.

[40] KUMAR A P, SUNTHARAVEL MUTHAIAH V M, MULA S. Effect of Nb, Y and Zr on thermal stability of nano-crystalline Al−4.5wt.% Cu alloy prepared by mechanical alloying [J]. Journal of Alloys and Compounds, 2017, 722: 617−627.

经 T6 和热暴露处理 WAAM-ZL205A 合金的析出相和力学性能演变

刘海江[1]，冯 艳[1,2]，彭超群[1,2]，蔡志勇[1,2]，王 檬[1]，李梓铭[1]，康智杰[1]，张晓笛[1]

1. 中南大学 材料科学与工程学院，长沙 410083；
2. 中南大学 高强结构材料科学与技术国家重点实验室，长沙 410083

摘 要：研究不同热暴露温度下 WAAM-ZL205A 合金的显微组织和力学性能，并将其与沉积态和 T6 态合金进行对比。与沉积态合金相比，T6 处理(535 ℃, 10 h) + (175 ℃, 10 h)合金的屈服强度增加至 366.9 MPa，这归因于细小、弥散的 θ″和 θ′相的析出强化，但伸长率降低至 12.9%。随着热暴露温度从 200 ℃升高至 300 ℃，合金的屈服强度显著下降，而达到性能稳定所需的时间缩短。300 ℃热暴露 24 h 后，晶界处部分 θ′相转变为 θ 相，晶内的 θ′相明显粗化，导致屈服强度降低至 188.9 MPa。当热暴露时间超过 120 h 后，合金的力学性能趋于稳定。

关键词：ZL205A 铝合金；析出相；力学性能；增材制造；热处理；热暴露；稳定性

(Edited by Wei-ping CHEN)